Supporting Information

An anion-sorted Li-ion electrolyte and flexible MnVO@SWCNT hybrid electrode for an efficient supercapacitor system

Ravikant Adalati[†,‡*], *Somdatta Singh*[‡], *Jakub Ćwiertnia*[1], *Dariusz Łukowiec*[§], *Dushyant Choudhary*[‡], *Marta Wala-Kapica*[†], *Wojciech Simka*[†], *Ramesh Chandra*[‡*], *Dawid Janas*[†*]

[†]Faculty of Chemistry, Silesian University of Technology, Krzywoustego 4, 44-100, Gliwice, Poland

[‡]Institute Instrumentation Centre, Indian Institute of Technology, Roorkee, 247667, Uttrakhand, India

[§]Materials Research Laboratory, Faculty of Mechanical Engineering, Silesian University of Technology, Konarskiego 18A, Gliwice 44-100, Poland

Email: ravikantad@gmail.com; ramesh.chandra@ic.iitr.ac.in; dawid.janas@polsl.pl

1. CV kinematics for the charge storage mechanism

Lindstrom and Randles-Sevcik methods were used to determine the charge storage mechanism. According to the method, the peak current (i_p) of the CV curve follows the scan rate (ν) [1]

$$i_p = a * \nu^b \tag{S1}$$

where a and b are adjustable variables and can be used to determine the capacitive or diffusive controlled charge storage kinematics of the electrode. From the Power law ($i \propto \nu$), the current is directly proportional to the scan rate for the simple system. For other complicated cases, the current is proportional to the square root of the scan rate ($\nu^{1/2}$), which insinuates the charge store via a diffusive-limited or intercalation/de-intercalation process [2,3].

$$i_p = (2.69 * 10^5) n^{3/2} A D_0^{1/2} C_0 \boldsymbol{\nu^{1/2}} \tag{S2}$$

Considering room temperature, C_0 represents the charge species' molar concentration, A signifies the electrode's active surface area, D_0 is the diffusion coefficient, and n is the number of transferred electrons. Further, Dunn et al. proposed the deconvolution of current into surface capacitive ($\propto \nu$) diffusive-limited intercalation process ($\propto \nu^{1/2}$) at any potential (V), as described in equations S3 and S4[4,5]

$$i(V) = k_1 v + k_2 \nu^{1/2} \tag{S3}$$

$$i(V)/\nu^{1/2} = k_1 \nu^{1/2} + k_2 \tag{S4}$$

where k_1 and k_2 are two constants and can be calculated by plotting equation S4 and comparing them with the straight-line equation ($y=m*x+c$). Slope and intercept of the plot $i(V)/\nu^{1/2}$ against $\nu^{1/2}$ deliver k_1 and k_2, respectively. These calculated values of constants (k_1 and k_2) offer a contribution of current via surface capacitive ($k_1 * \nu$) and diffusive limited ($k_2 * \nu^{1/2}$) at any potential for all the scan rates[6–8].

2. Electrochemical parameter calculation

The capacitance (C_A) is calculated from charging/discharging curves using equation S5 [9,10]

$$C_A\ (F cm^{-2}) = \frac{\boldsymbol{2*I}}{\boldsymbol{A*\Delta V}} \int \boldsymbol{V\,dt} \tag{S5}$$

where I (mA), A (cm^2), ΔV (V), and $\int \boldsymbol{V\,dt}$ are the constant discharging current, area of the active electrode, discharge potential after IR drop, and integral area under the GCD curve (discharge time).

The Coulombic efficiency ($\eta\%$) of FASC is calculated using equation S6

$$\eta(\%) = \frac{t_d}{t_c} \quad \text{(S6)}$$

where t_d is the discharging time and t_c is the charging time.

The energy density (E) and power density (P) were calculated using equations S7 and S8[11]

$$E\ (Whcm^{-2}) = \frac{\mathbf{0.5} * \boldsymbol{C_A} * (\boldsymbol{\Delta V})^{\mathbf{2}}}{\mathbf{3600}} \quad \text{(S7)}$$

$$P\ (Wcm^{-2}) = \frac{\boldsymbol{E}*\mathbf{3600}}{\boldsymbol{\Delta T}} \quad \text{(S8)}$$

where C_A ($F\ cm^{-2}$) and ΔT (s) are the areal capacitance of NC-FSC and discharge time.

3. X-ray Diffractogram

The crystalline structure of the MnVO and MnVO@SWCNT was verified by XRD analysis (**Figure S1**) along with the diffractogram of the selected range in the inset. XRD confirmed the $Mn_2V_2O_7$ formation, crystalline structure, with the monoclinic crystal system, as attributed in the JCPDS card no. 00-022-0436. Extra peaks at 43° and 44° for MnVO@SWCNT matched SWCNT diffraction patterns, suggesting their incorporation with BTMO [12,13]. The high intensity of these peaks is due to the large amount of SWCNT (mesh) compared to MnVO particles. As confirmed by XRD analysis, the presence of SWCNTs can improve conductivity and offer electrochemical processes active sites for electrochemical processes in hybrid electrodes, which affects charge transfer kinetics and stability.

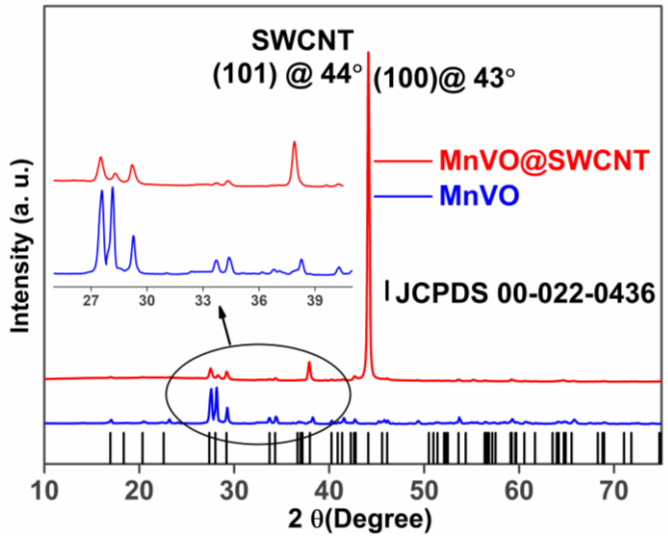

Figure S1 *XRD diffractogram of MnVO powder and MnVO@SWCNT hybrid electrode.*

4. Topography analysis

The topography analysis of the MnVO powder pattern is displayed in **Figure S2** with high-resolution transmission electron microscopy (HRTEM) and selected area electron diffraction (SAED). In **Figure S2**(a), an image of the MnVO powder shows a cube-like nano-structure growth, consistent with the structure seen in SEM images. **Figure S2**(b) visualizes elemental analysis at multiple sample locations, which confirms the presence of required elements without impurity, as confirmed by the SEM-EDS and XPS analysis. In **Figure S2**(c), d-spacing was evaluated using developed fringes in the HRTEM image. This d-spacing perfectly matched the present crystalline planes in the material with a monoclinic crystal system consistent with XRD. The SAED analysis in **Figure S2**(d) indicated that the BTMO material was made up of polycrystalline diffraction characteristics with good crystallinity, as confirmed by the XRD diffractogram.

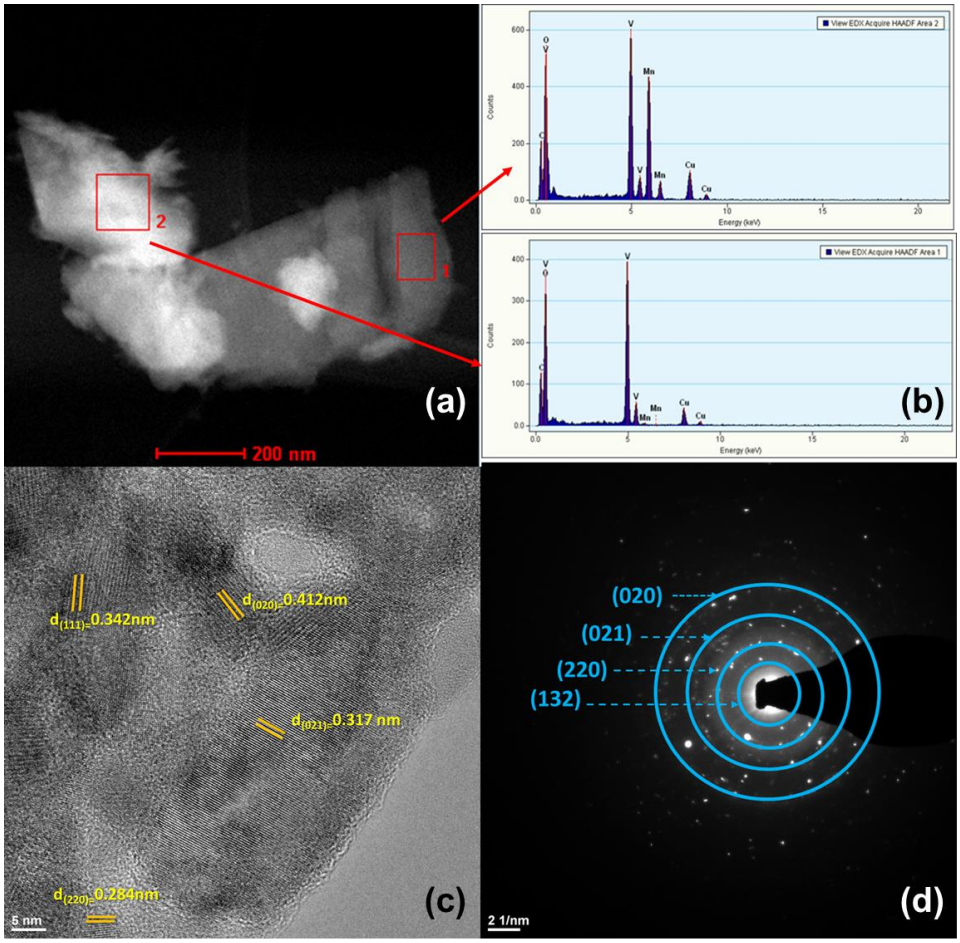

Figure S2 *Surface topography of MnVO powder (a) TEM image, (b) TEM EDS spectra, and (c) HRTEM image, as well as (d) SAED pattern.*

5. Electrochemical study of the electrodes

In the study of MnVO@SWCNT in various electrolytes, it was observed that MnVO@SWCNT performed better with LiOH electrolyte compared to other anion salts combined with Li. To demonstrate the improvement by incorporating MnVO in the SWCNT to create a hybrid electrode, CV curves at a scan rate of 100 mV cm^{-2} are shown in **Figure S3(a)**. The increased integrated area confirmed the influence of MnVO in increasing the capacitive performance of the hybrid electrode. The fabricated hybrid electrode offered five times more capacitance than bare SWCNT in 1 M LiOH aqueous electrolyte, as presented in the calculated areal capacitance values in **Figure S3(b)**. This increase in capacitance could be attributed to the presence of the metal oxide combination of Mn and V with several oxidation states. These oxidation states offered strong reduction and oxidation peaks in CV (higher current value or more charge transfer/movement), but due to the many oxidation states, it was difficult to distinguish between peaks. Consequently, the CV curve appeared symmetrical without any distinct peaks, but with increased integrated area due to more movement of charges[14]. Further, for more information, volumetric capacitances were also calculated by using electrode thickness as presented in Figure S5 (b). The volumetric capacitance exhibits almost the same enhancement as the areal capacitance, because of the thickness of the electrodes, which are almost the same, 0.0040 cm and 0.0048 cm for SWCNT and MnVO@SWCNT sheet electrodes, respectively. For the galvanostatic capacitance, the weight of the 1 cm^2 electrodes was found to be 1.85 mg for MnVO@SWCNT and 1.02 mg for the SWCNT.

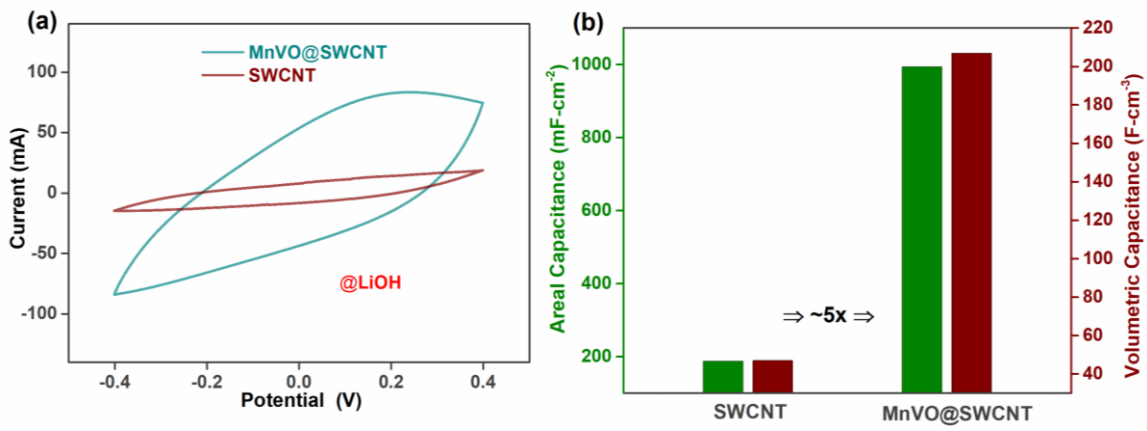

Figure S3 *(a) CV curves at 100 mV cm^{-2} of bare SWCNT and hybrid MnVO@SWCNT electrode, and (b) calculated capacitance for comparison.*

5.1 CV kinetic and galvanostatic electrochemical analysis of electrodes

To gain more insight into the charge storage mechanism of the hybrid electrode, a study was conducted by analyzing CV kinematics. **Figure S4(a-c)** presents the CV kinematics of the hybrid electrode. For comparison, the same study for a bare SWCNT electrode is shown in **Figure S4(d-f)**. The hybrid electrode demonstrated a more capacitive (surface) charge storage mechanism, around 87.95%, compared to the bare SWCNT (only 45.55%) at a high scan rate of 200 mV s^{-1}. The higher surface charge storage capacity of the hybrid electrode was due to the inclusion of BTMO (metal oxide material), which offered a larger surface area to the electrode. This increase in the surface charge storage mechanism led to improved charge storage and electrode stability. However, with anions, the charge storage mechanism appeared to be similar, with a very slight difference, as per our calculation and analysis. These similarities may be due to the dominant charge storage by the Li-ion, which has a wider hydrated ionic radius (3.82 Å) compared to all anions (Cl^-, NO_3^-, OH^-, and SO_4^{2-})[15]. Anions play an important role in ion mobility, whether the charge is stored by capacitive (surface) or diffusive (bulk) mechanisms.[16,17]. This study shows a significant contribution of the diffusive-limited intercalation process in bare SWCNT sheet electrodes, indicating that the stored charges mostly originate from the diffusive intercalation of electrolyte ions on the wall of SWCNTs. The prevalence of the capacitive process in the overall charge storage mechanism in the hybrid electrode due to the dominance of charge species at the surface can be explained by the electrode's pseudocapacitive behavior acquired from the MnVO particles.

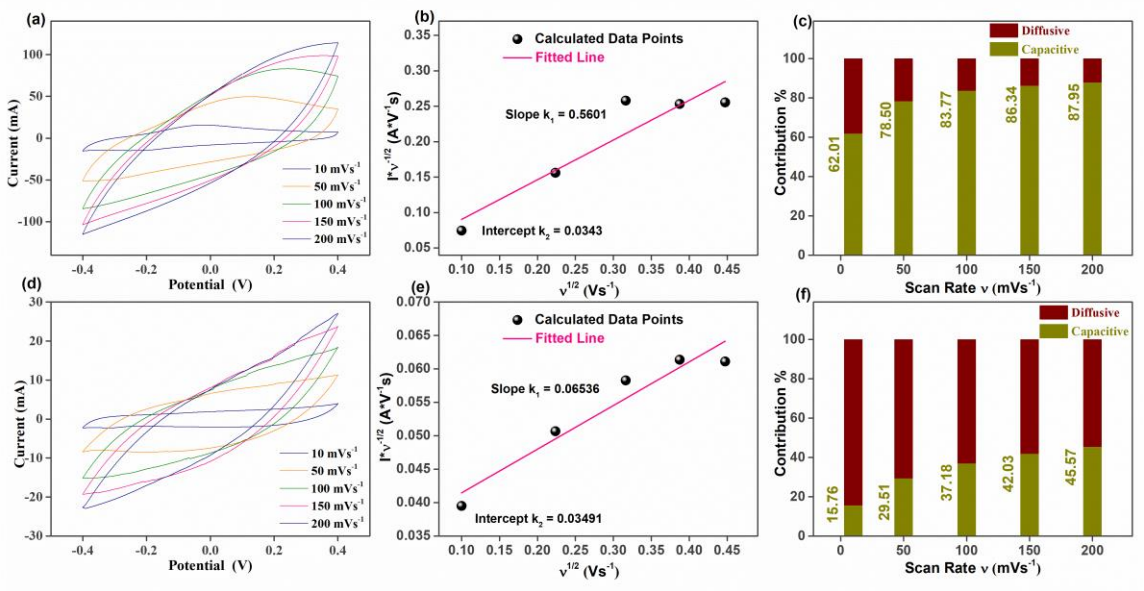

Figure S4 *CV kinematics of the (a-c) hybrid electrode, and (d-f) bare SWCNT sheet.*

5.2 Galvanostatic charge-discharge (GCD) *analysis of electrodes*

To better understand the effect of anions on the electrochemical properties of the hybrid electrode, galvanostatic charge-discharge (GCD) was performed at various current densities in the presence of varying Li-electrolytes with anions. GCD curves in different electrolytes were symmetric and showed reversible capacitive performance as presented in **Figure S5(a-d)**. The GCD data for the LiOH electrolyte (**Figure S5(c)**) exhibited curves representing a shape of a more pseudocapacitive and hybrid nature of charge storage mechanism compared to other electrolytes (LiCl, $LiNO_3$, and Li_2SO_4). This plateau-type/non-triangle symmetric curve confirmed the hybrid nature of the electrode and resulted in the increment of discharging time, ultimately enhancing capacitance, due to the presence of a high number of hydroxide anions (OH^-) from electrolyte salt with high ionic conduction and mobility in water-based electrolyte [18]. The high performance of the hybrid electrode in LiOH was also confirmed by calculated capacitive parameters (Areal capacitance, Coulombic efficiency, Energy Density) by using GCD curves. All the calculations were done after considering the IR drop of the GCD curves.

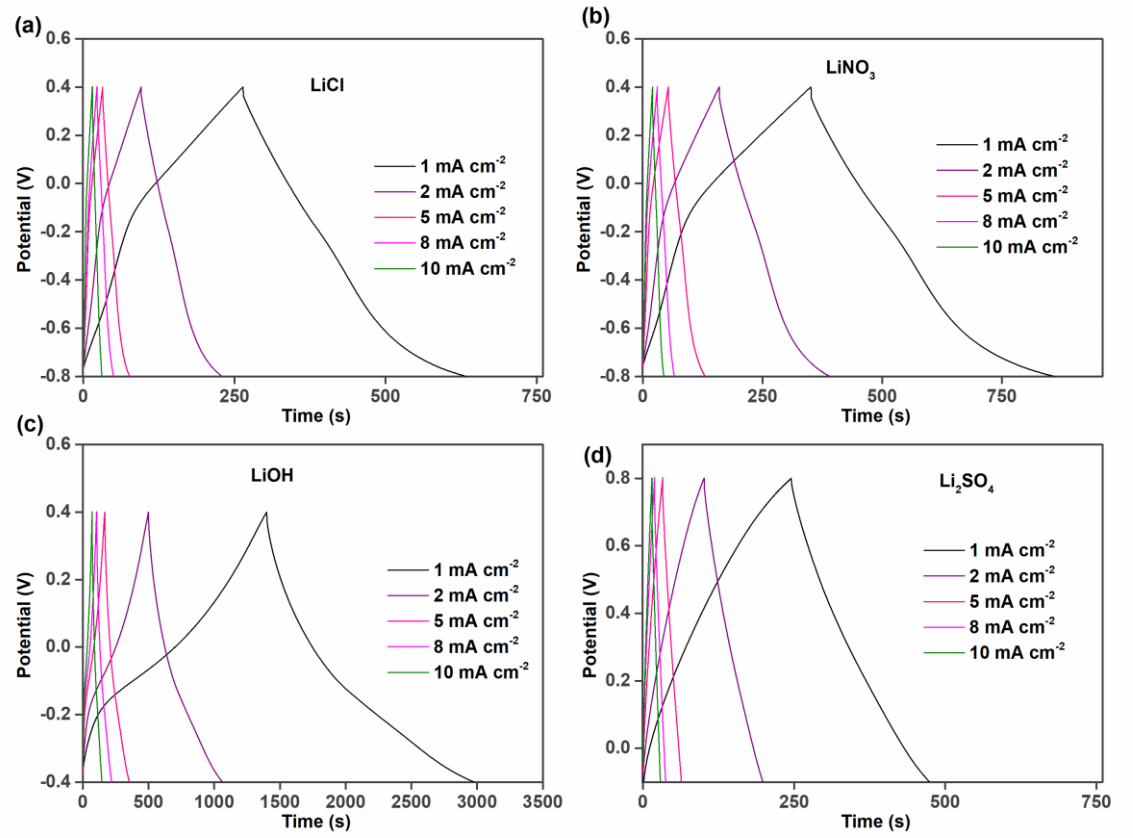

Figure S5 *GCD curves at various current densities of the hybrid electrode in 1 M electrolyte of (a) LiCl, (b) $LiNO_3$, (c) LiOH, and (d) Li_2SO_4.*

5.3 Post-electrochemical surface analysis of electrodes

Figure S6 (a-d) depicts the top-view SEM micrographs of the electrochemically treated hybrid electrode in anion-selected electrolytes. These micrographs display the preserved structure of the electrode, confirming that the MnVO@SWCNT hybrid electrode has structural integrity even after electrochemical treatment. As shown in **Figure S6**(c), the surface structure was similar to the initial electrode and exhibited a spaghetti-type structure with the addition of clear white particles. These white particles may arise due to the formation of the MnOOLi, as a result of the MnVO nanoparticle chemical reaction with the LiOH electrolyte.

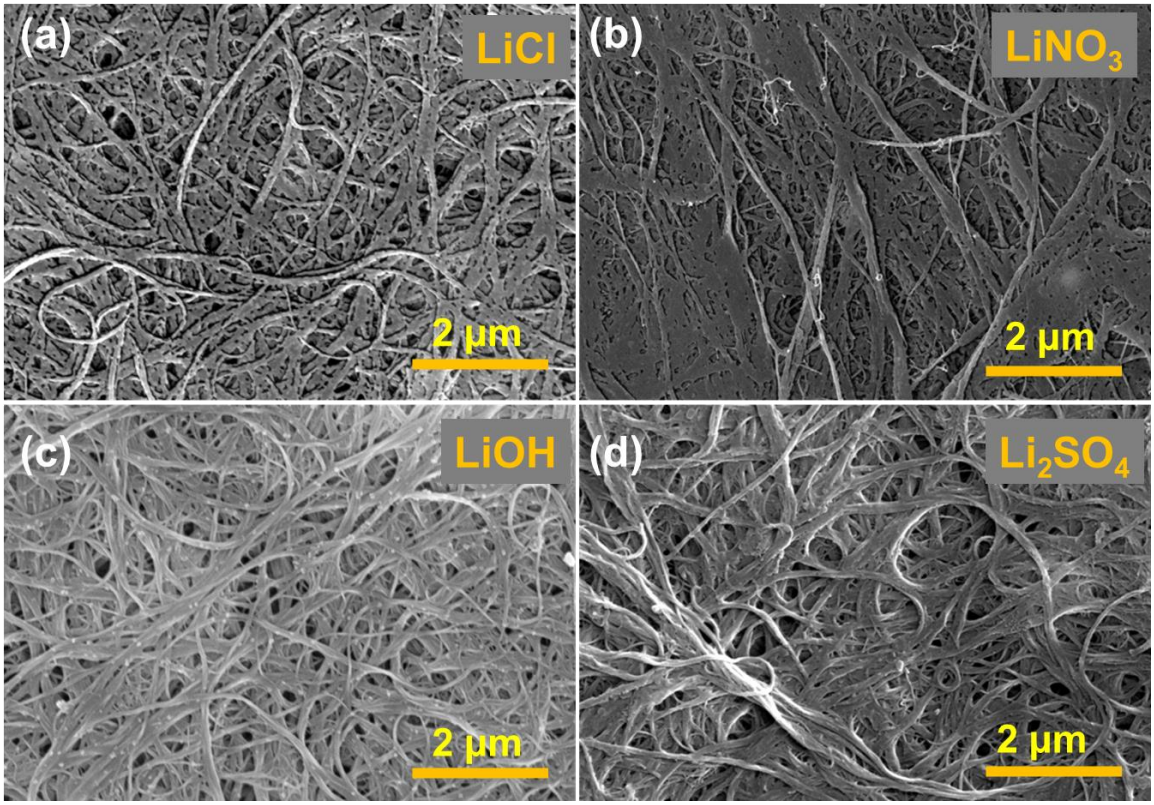

Figure S6 *Surface micrographs of the hybrid electrode after electrochemical study in (a) LiCl, (b) $LiNO_3$, (c) LiOH, and (d) Li_2SO_4.*

References

[1] A. Cymann-Sachajdak, M. Graczyk-Zajac, G. Trykowski, M. Wilamowska-Zawłocka, Understanding the capacitance of thin composite films based on conducting polymer and carbon nanostructures in aqueous electrolytes, Electrochim Acta 383 (2021) 138356. https://doi.org/10.1016/j.electacta.2021.138356.

[2] Z. Wang, H. Wang, S. Ji, X. Wang, P. Zhou, S. Huo, V. Linkov, R. Wang, Hollow-structured NiCoP nanorods as high-performance electrodes for asymmetric supercapacitors, Mater Des 193 (2020) 108807. https://doi.org/10.1016/j.matdes.2020.108807.

[3] Y. Li, L. Xu, M.Y. Jia, L. Cui, X. Liu, X.J. Jin, Fabrication of Pd Nanocubes@CdIF-8 catalysts for highly efficient electrocatalytic sensing of H2O2 and high-performance supercapacitor, Mater Des 186 (2020) 108267. https://doi.org/10.1016/j.matdes.2019.108267.

[4] Y. Jiang, J. Liu, Definitions of Pseudocapacitive Materials: A Brief Review, Energy and Environmental Materials 2 (2019) 30–37. https://doi.org/10.1002/eem2.12028.

[5] M. Singh, A. Sahoo, K.L. Yadav, Y. Sharma, Role of magnetism present in the cobaltites (ACo2O4, A = Co, Mn, and Fe) on the charge storage mechanism in aqueous supercapacitor, Appl Surf Sci 568 (2021) 150966. https://doi.org/10.1016/j.apsusc.2021.150966.

[6] M. Forghani, S.W. Donne, Method Comparison for Deconvoluting Capacitive and Pseudo-Capacitive Contributions to Electrochemical Capacitor Electrode Behavior, J Electrochem Soc 165 (2018) A664–A673. https://doi.org/10.1149/2.0931803jes.

[7] J. Wang, J. Polleux, J. Lim, B. Dunn, Pseudocapacitive contributions to electrochemical energy storage in TiO 2 (anatase) nanoparticles, Journal of Physical Chemistry C 111 (2007) 14925–14931. https://doi.org/10.1021/jp074464w.

[8] H. Liu, D. Zhao, P. Hu, K. Chen, X. Wu, D. Xue, Design strategies toward achieving high-performance CoMoO4@Co1.62Mo6S8 electrode materials, Materials Today Physics 13 (2020). https://doi.org/10.1016/j.mtphys.2020.100197.

[9] A. Kumar, A. Sanger, A. Kumar, R. Chandra, Single-step growth of pyramidally textured NiO nanostructures with improved supercapacitive properties, Int J Hydrogen Energy 42 (2017) 6080–6087. https://doi.org/10.1016/j.ijhydene.2016.11.036.

[10] D.D. Nguyen, C.H. Hsiao, T.Y. Su, P.Y. Hsieh, Y.L. Chen, Y.L. Chueh, C.Y. Lee, N.H. Tai, Bioinspired networks consisting of spongy carbon wrapped by graphene sheath for flexible transparent supercapacitors, Commun Chem 2 (2019) 1–10. https://doi.org/10.1038/s42004-019-0238-9.

[11] Q. Zhang, X. Wang, Z. Pan, J. Sun, J. Zhao, J. Zhang, C. Zhang, L. Tang, J. Luo, B. Song, Z. Zhang, W. Lu, Q. Li, Y. Zhang, Y. Yao, Wrapping Aligned Carbon Nanotube Composite Sheets around Vanadium Nitride Nanowire Arrays for Asymmetric Coaxial Fiber-Shaped Supercapacitors with Ultrahigh Energy Density, Nano Lett 17 (2017) 2719–2726. https://doi.org/10.1021/acs.nanolett.7b00854.

[12] K. Manna, S.K. Srivastava, Contrasting Role of Defect-Induced Carbon Nanotubes in Electromagnetic Interference Shielding, Journal of Physical Chemistry C 122 (2018) 19913–19920. https://doi.org/10.1021/acs.jpcc.8b04813.

[13] A. Cao, C. Xu, J. Liang, D. Wu, B. Wei, X-Ray Diffraction Characterization on the Alignment Degree of Carbon Nanotubes. Chemical Physics Letters, Volume 344, Issues 1–2, 2001, https://doi.org/10.1016/S0009-2614(01)00671-6

[14] Y. Gogotsi, R.M. Penner, Energy Storage in Nanomaterials - Capacitive, Pseudocapacitive, or Battery-like?, ACS Nano 12 (2018) 2081–2083. https://doi.org/10.1021/acsnano.8b01914.

[15] Y. Zhu, H. Pham, J. Park, A New Aspect of the Li Diffusion Enhancement Mechanism of Ultrathin Coating Layer on Electrode Materials, ACS Appl Mater Interfaces 11 (2019) 38719–38726. https://doi.org/10.1021/acsami.9b12740.

[16] A. Olean-Oliveira, G.A. Oliveira Brito, C.X. Cardoso, M.F.S. Teixeira, Role of anion size in the electrochemical performance of a Poly(thionine) redox conductive polymer using electrochemical impedance spectroscopy, Polymer (Guildf) 258 (2022). https://doi.org/10.1016/j.polymer.2022.125291.

[17] R. Kumar, P. Rai, A. Sharma, Free-standing NiV2S4 nanosheet arrays on a 3D Ni framework: Via an anion exchange reaction as a novel electrode for asymmetric supercapacitor applications, J Mater Chem A Mater 4 (2016) 17512–17520. https://doi.org/10.1039/c6ta07171f.

[18] Y. Shao, M.F. El-Kady, J. Sun, Y. Li, Q. Zhang, M. Zhu, H. Wang, B. Dunn, R.B. Kaner, Design and Mechanisms of Asymmetric Supercapacitors, Chem Rev 118 (2018) 9233–9280. https://doi.org/10.1021/acs.chemrev.8b00252.